

## A Cloud Fraction versus View Angle Technique for Automatic In-Scene Evaluation of the MISR Cloud Mask

GUANGYU ZHAO AND LARRY DI GIROLAMO

*Department of Atmospheric Sciences, University of Illinois at Urbana-Champaign, Urbana, Illinois*

(Manuscript received 11 July 2003, in final form 3 December 2003)

### ABSTRACT

The Multiangle Imaging Spectroradiometer (MISR), on board the Earth Observing System (EOS) satellite *Terra*, is the first high-resolution imager to make global, near-simultaneous multispectral and multiangle radiometric measurements of the earth. A standard product of MISR is the radiometric camera-by-camera cloud mask (RCCM), which provides a cloud mask for each of the nine MISR cameras. Validation of the RCCM is ongoing, and in this paper an automatic and efficient technique is described that is being used to flag scenes for which the quality of the RCCM may be suspect, thus allowing rapid convergence toward validation. The technique, herein called the  $F_{\theta}$  technique, makes use of the physical relationship that cloudiness increases with viewing obliquity. Where this behavior is not met for a given scene, the  $F_{\theta}$  technique flags the scene as potentially problematic. The technique is applied to  $\sim 4$  months of MISR data to demonstrate its utility and to identify common problems that exist in version F01.0010 of the RCCM. In the course of research into the  $F_{\theta}$  technique, the existence of greater radiative and spatial contrast between clear and cloudy pixels in oblique views that measure radiation in the forward-scatter direction, as compared with oblique views that measure radiation in the backscatter direction, have been observed. As a result, thinner clouds can be detected in views that measure radiation in the forward-scatter direction as compared with oblique views that measure radiation in the backscatter direction for a given air mass. It is hypothesized that a similar effect must exist with other cloud detection techniques using radiative and spatial measures constructed from solar channels. It is shown that this effect manifests itself as a unique angular signature in the MISR RCCM that may be exploited to flag scenes as potentially being dominated by thin cirrus or a thick haze.

### 1. Introduction

A cloud mask classifies satellite instantaneous fields of view (pixels) as either clear or cloudy, with some recent cloud masks also assigning a measure of confidence to the mask (e.g., Gustafson et al. 1994, Ackerman et al. 1998, Diner et al. 1999). It is an initial input to most space-based remote sensing algorithms for retrieving atmospheric and surface properties [e.g., vegetation index (Tarpley et al. 1984), sea surface temperature (McClain 1989), aerosol and water vapor properties (King et al. 1992), and cloud optical and microphysical properties (Platnick et al. 2003)]. Therefore, a quality cloud mask is critical for the successful retrieval of many geophysical products. Although there are numerous cloud-masking algorithms [see, e.g., Goodman and Henderson-Sellers (1988) for a review], the approaches taken to evaluate those algorithms are very limited, and may be generically classified into four types: 1) manual inspections of the cloud mask against

the satellite radiance images used in computing the cloud mask, 2) comparisons between satellite observation and collocated surface or in situ measurements (e.g., Minnis and Harrison 1984), 3) comparisons between different satellite observations (e.g., Stowe et al. 1988), and 4) comparisons between satellite observations and cloud climatologies (e.g., Stowe et al. 1988). Type 1 is the most reliable, but exceedingly tedious and time consuming, making it difficult for global evaluation. Types 2 and 3 require spatial consistency and temporal coincidence among different datasets that are often difficult to satisfy. Type 4 only offers a general evaluation on cloud mask performances over large spatial and temporal scales; hence, it cannot return any useful information on the quality of the cloud mask at a particular location and time.

The purpose of this article is to introduce another type of evaluation technique that is unique to the Multiangle Imaging Spectroradiometer (MISR) on board the Earth Observing System (EOS) satellite *Terra*. This evaluation technique examines the nine cloud fractions derived from the nine separate MISR cameras (see section 2 for instrument description) that are registered to the same scene. Cloud fraction is calculated for each camera as the ratio of the number of cloudy pixels to

---

*Corresponding author address:* Guangyu Zhao, Department of Atmospheric Sciences, University of Illinois at Urbana-Champaign, Urbana, IL 61801.  
E-mail: gyzhao@atmos.uiuc.edu

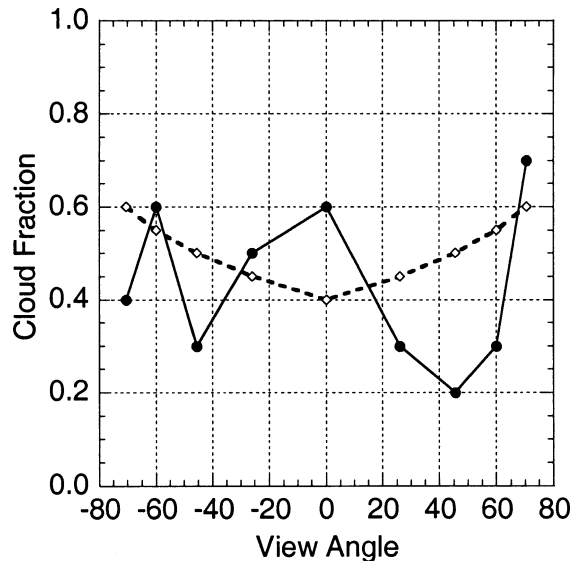


FIG. 1. Cloud fraction as a function of camera view angle. The dashed line represents an ideal case. The solid line represents a case with unreliable cloud masks. Symbols represent positions of the MISR view angles. Negative values of view angle are for the forward bank of MISR cameras, and positive values are for the aft bank. This figure is a representative example, rather than specific observations.

the number of total pixels of a scene. Ideally, the cloud fraction should increase with viewing zenith angle, largely as a consequence of an increase in the amount of cloud sides observed (e.g., Snow et al. 1985, Minnis 1989). Therefore, by plotting the cloud fraction as a function of camera view angle, we should expect a curve with similar behavior as the dashed line shown in Fig. 1; that is, cameras with more oblique viewing zenith angles should detect more clouds, and cameras with the same viewing zenith angle should detect similar amounts of cloud. If, however, the behavior of the cloud fraction with view angle does not represent a physical possibility, like the solid line shown in Fig. 1, then the scene should be flagged as having an unreliable cloud mask. Such flagged scenes can then be examined in more detail for diagnosing and improving the cloud mask algorithm. The intent of this article is to derive and demonstrate a technique to automatically flag these potentially problematic scenes (PPS). In doing so, we discover an interesting relationship between view angle and our ability to detect thin clouds.

This article is divided into six sections. Section 2 briefly introduces the MISR instrument and its cloud masks. The definitions of cloud and cloud fraction are discussed in section 3. The  $F_{\theta}$  technique and its application to MISR data are described in section 4. Section 5 shows the experimental results, and section 6 concludes our study.

## 2. MISR and its cloud masks

MISR is the first high-resolution imager to make global, near-simultaneous multispectral and multiangle ra-

diometric measurements of the earth. Details of the MISR instrument and its performance can be found in Diner et al. (1998 and 2002, respectively). In brief, nine separate cameras provide viewing zenith angles relative to the surface reference ellipsoid of  $0^{\circ}$ ,  $26.1^{\circ}$ ,  $45.6^{\circ}$ ,  $60.0^{\circ}$ , and  $70.5^{\circ}$ , with one camera (designated AN) pointing toward the nadir, one bank of four cameras (designated AF, BF, CF, and DF in order of increasing off-nadir angle) pointing forward in the along-track orbital direction, and one bank of four cameras (designated AA, BA, CA, and DA) pointing in the backward direction. It takes approximately 7 min to view a given scene from all nine cameras. Each camera has four narrow spectral bands centered at 446, 558, 672, and 866 nm. From its 705-km orbit, the AN camera has a spatial resolution of 250 m and a swath width of 376 km. All other cameras are designed to give a cross-track resolution of 275 m with a swath width of 413 km. MISR is on the EOS *Terra*, which is sun synchronized and crosses the equator at  $\sim 1030$  LT from north to south.

MISR operational processing generates three independent cloud masks: the radiometric camera-by-camera cloud mask (RCCM), the stereoscopically derived cloud mask (SDCM), and the angular signature cloud mask (ASCM). The RCCM is generated for each of the nine cameras using radiometric information collected within each camera; hence, each region on earth has nine RCCMs. The SDCM and the ASCM make use of information from multiple cameras to achieve a single SDCM and ASCM product for each region on earth. As such, the proposed cloud fraction versus view angle technique (hereinafter, the  $F_{\theta}$  technique) for flagging a scene as PPS is only applicable to the RCCM.

Details of the RCCM algorithm can be found in Diner et al. (1999). The RCCM algorithm can be divided into land and ocean algorithms. As of this writing, the RCCM land algorithm has not yet been fully implemented into operational processing; only the RCCM ocean algorithm is fully implemented. Therefore, the  $F_{\theta}$  technique derived herein is only demonstrated on the RCCM ocean product, but it will be equally applicable to the RCCM land product.

In brief, the observables used to generate the RCCM over an ocean are the bidirectional reflectance factor (BRF) in the near-IR band (hereinafter, NIR) at 1.1-km resolution, and the standard deviation ( $\sigma$ ) of the  $4 \times 4$  array of the 275-m red band BRF within a 1.1-km area. The NIR BRF and  $\sigma$  for each 1.1-km resolution pixel are each tested against three thresholds to classify a pixel as high-confidence cloudy, low-confidence cloudy, low-confidence clear, or high-confidence clear. The two tests may return different results, and the final cloud mask is determined from the logical combination of the results of two tests as described in Diner et al. (1999). Because there are only two tests, the RCCM is very sensitive to the choice of thresholds. Fully taking into account the fact that the thresholds are a function of sun/viewing geometry (solar zenith angle, viewing zenith angle, and

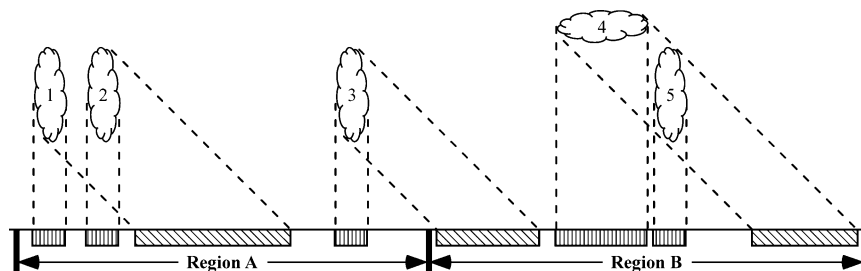


FIG. 2. An illustration depicting three geometrical factors that may affect how cloud fraction changes with viewing zenith angle, as described in the main text. The vertical and slanted hatches depict areas of the surface that are obscured by clouds when viewed from space in nadir and oblique viewing directions, respectively.

relative azimuth angle), the RCCM algorithm breaks the ranges of solar zenith angle, viewing zenith angle, and relative azimuth angle into 10, 5, and 12 bins, respectively. Initial thresholds for each bin were manually derived in the same manner from time-cumulated statistics using 135 MISR orbits over the period from May to August 2000 as described in Zhao (2003). The total number of thresholds is, therefore, 5 (viewing zenith angle)  $\times$  12 (relative azimuth angle)  $\times$  10 (solar zenith angle)  $\times$  3 (threshold type)  $\times$  2 (observable) = 3600. The quality of the RCCM relies on the validity of the 3600 thresholds. In practice, it takes an experienced person about a day to manually tune up and verify a threshold. Hence, it would take the better part of a decade to manually verify all of the thresholds. Over land, this verification problem is compounded by the fact that there are 3600 thresholds [but of two different observed quantities: a parameter  $D$  derived from the normalized difference vegetation index (NDVI) and the band-3 reflectance, and the  $D$  spatial variability index] for each of the 1580 land surface regions that are derived dynamically every 16 days (Diner et al. 1999). With the application of the  $F_{\theta}$  technique, the time spent on evaluating thresholds is now considerably reduced by focusing only on those thresholds that cause poor performances in the RCCM.

### 3. Defining clouds and cloud fraction

Before examining the  $F_{\theta}$  technique, a brief review on how clouds and cloud fraction are defined, and how these definitions impact the MISR observations of cloudiness, is given in this section.

In satellite remote sensing, the long-standing question of “what is a cloud?” continues to be debated, because no precise quantitative definition on what constitutes a cloud presently exists (Di Girolamo and Davies 1997). For example, how thin does a cloud have to be before it is too thin to be considered a cloud? Ultimately, it is the minimum detectable optical depth  $\tau_{\min}$  that defines the existence of the cloud for a given cloud detection algorithm applied to a given instrument. Theoretically,  $\tau_{\min}$  is expected to depend on the underlying surface

type, the concentrations and types of atmospheric gases and aerosols, the single scattering properties of clouds, and the sun-view geometry. Di Girolamo and Davies (1994) were the first to suggest that a conservative  $\tau_{\min}$  (i.e., such that no clear pixels are labeled cloudy, otherwise  $\tau_{\min}$  may be infinitely close to 0) should be reported as part of any satellite cloud detection algorithm. The importance in doing so is to help to reconcile differences in cloud amount climatologies derived from different satellite cloud detection algorithms, given that algorithms with lower  $\tau_{\min}$  produce higher cloud amounts. Although the intent of this paper is not to derive the  $\tau_{\min}$  of the MISR RCCM, which is part of the larger MISR cloud mask validation effort, we show observational evidence from MISR that  $\tau_{\min}$  is a function of the sun-view geometry.

From an observational point of view, cloud fraction is defined as the fraction of background that is obscured by clouds (Henderson-Sellers and McGuffie 1990). For a surface observer reporting cloud fraction, the background is some imaginary sky dome. For a satellite sensor, the background is the earth’s surface from the viewing direction of the satellite sensor. The definition of cloud fraction employed in climate modeling is equivalent to that of a nadir-viewing satellite instrument. However, very few satellite observations are made at nadir. Even for perfect cloud detection, cloud fraction between nadir and oblique views from space may differ because of the following effects, all of which can be directly observed by MISR: 1) cloud geometric thickness, 2) out-of-region parallax, 3) multilayered cloud shadowing, and 4) expansion of the ground-instantaneous field of view (GIFOV) of the observing instrument. Figure 2 illustrates the first three effects by depicting a number of clouds (labeled 1–5) that fall over two neighboring regions (labeled region A and B). Note that 1) the region A cloud fraction contribution from clouds 1 and 2 increases with viewing obliquity due to the geometrical thickness of the clouds; 2) out-of-region parallax may occur for cloud 3, whereby cloud 3 contributes to the region A cloud fraction for nadir views, but for certain oblique views it contributes to the region B cloud fraction; and 3) multilayered cloud shadowing

occurs for clouds 4 and 5 for certain views, which may contribute to a lower region B cloud fraction than at nadir, as in the example shown.

For an instrument with a fixed IFOV, the GIFOVs expand with viewing obliquity. If cloud fraction is calculated as the fraction of cloudy GIFOVs over a given region, then cloud fraction overestimation will be larger for larger GIFOVs, assuming perfect cloud detection (Di Girolamo and Davies 1997). For MISR, the GIFOVs expand only in the along-track orbital direction. It is largest for the most oblique views, where the GIFOV is  $275 \text{ m} \times 707 \text{ m}$ . With the ground-sampling interval being  $275 \text{ m}$ , averaging  $4 \times 4$  pixels (as done in the RCCM BRFT test discussed in section 2) leads to a GIFOV of  $1.1 \text{ km} \times 1.53 \text{ km}$ . Relative to a  $1.1 \text{ km} \times 1.1 \text{ km}$  GIFOV, the cloud fraction from a  $1.1 \text{ km} \times 1.53 \text{ km}$  GIFOV is expected to cause an overestimate of only 1%–2% based on the results of Wielicki and Parker (1992) for their  $0.83\text{-}\mu\text{m}$  radiance threshold test. As will become evident in the following sections, this effect is negligible in the application of the  $F_\theta$  technique.

In addition to these effects, the cloud fraction between nadir and oblique views may be different because of effects of imperfect cloud detection, namely, 1) an increase in  $\tau_{\text{min}}$  with viewing obliquity due to an increase in the optical path, and 2) errors in cloud detection. The  $F_\theta$  technique described in the next section is an automated technique to identify potential errors in MISR cloud detection by examining the behavior of cloud fraction versus view angle.

One final effect that is specific to MISR is the  $\sim 7$  min of time needed to view a given scene from all nine cameras. During this time, cloud coverage may increase or decrease. The  $F_\theta$  technique will identify cases in which this effect is significant, although the likelihood that it is significant is extremely small, given that no such cases were observed (section 5).

#### 4. The $F_\theta$ technique

In MISR terminology, an orbit is a Pole-to-Pole swath of data of the daylight side of the earth. Each orbit is divided into 180 blocks, where a block is approximately  $140.8 \text{ km}$  in the along-track direction. For the purpose of the  $F_\theta$  technique, we define a scene as five MISR blocks [ $\sim 360 \text{ km}$  (swath width)  $\times 704 \text{ km}$  (along-track length)], and the cloud fractions for each of the nine MISR cameras are calculated over a scene. A five-block scene is large enough to neglect the out-of-region parallax and multilayered cloud-shadowing effects on the view angle dependence of cloud fraction, as discussed in section 3, if the distribution of individual clouds over this region are considered random. (We have not observed these two effects to have a significant impact on the behavior of cloud fraction vs angle over a five-block region. This is not the case for a one-block region.) Simultaneously, a five-block scene is small enough to

contain only one or two threshold bins, which makes it easy to trace thresholds once a scene is marked as PPS.

The MISR operational processing takes the  $1.1\text{-km}$  resolution RCCM results and calculates cloud fractions over  $17.6 \text{ km} \times 17.6 \text{ km}$  regions. They are stored into the MISR cloud classifier product, along with other information such as land fraction, no retrieval fraction, etc. Thus, to save processing time, the cloud fraction over the five-block scene used in the  $F_\theta$  technique is calculated from the MISR cloud classifier product rather than the original RCCM product.

One factor that needs to be considered before processing the data is the zonal shift in the MISR swath from one camera to another. The zonal shift occurs because there is transition time between two different cameras viewing the same scene (the transition time between the DF and DA cameras is  $\sim 7$  min). The rotation of the earth within the transition time causes part of the scene viewed by one camera to be zonally shifted relative to another camera. The result is that only part of the swath collected from one camera overlaps with the swath of another camera. In order to plot the cloud fraction versus view angle correctly for the  $F_\theta$  technique, cloud fractions need to be defined only for the common area viewed by all nine cameras. Between  $55^\circ\text{N}$  and  $55^\circ\text{S}$ , the overlap region of all nine cameras ranges from approximately  $335$  to  $355 \text{ km}$  for a horizontal line in the space oblique Mercator (SOM) projection. The SOM projection is used to register the radiances from all nine MISR cameras (Bothwell et al. 2002).

The  $F_\theta$  procedure for flagging a MISR scene as PPS is as follows:

- 1) Read in five blocks of MISR cloud classifier data.
- 2) Retrieve the land fraction of each  $17.6 \text{ km} \times 17.6 \text{ km}$  region. If the total land fraction over the five-block scene is larger than 50%, then repeat step 1 for the next five blocks. Otherwise, go to step 3. A 50% land fraction threshold was used for the following reason. As of this writing, the RCCM land algorithm is not fully operational. Therefore, cloud fraction is calculated from all cameras over the ocean only. However, because of parallax caused by different views of the same scene, it is possible that a cloud viewed by one camera is over the ocean but over land when viewed by another camera. Experiments demonstrate that choosing a five-block scene with less than 50% land fraction is enough to neglect the errors incurred in the ocean cloud fractions due to this parallax effect. This step should of course be omitted when the RCCM land algorithm becomes fully operational.
- 3) Retrieve the low-confidence cloud, high-confidence cloud, and no-retrieval fractions for all nine cameras for each  $17.6 \text{ km} \times 17.6 \text{ km}$  region. The total cloud fraction is the sum of low- and high-confidence cloud fractions. [The RCCM was designed to have the best delineation between clear sky and clouds occurring

between low-confidence clear sky and low-confidence clouds. This is different than the MODIS cloud mask (Ackerman et al. 1998), where confidence levels are more closely tied to how clear a pixel is.] Define the common swath width for all nine cameras and discard nonoverlap regions. The total cloud fraction for each camera is calculated by averaging the cloud fraction value of each  $17.6 \text{ km} \times 17.6 \text{ km}$  region within the common swath over the five-block scene. If a  $17.6 \text{ km} \times 17.6 \text{ km}$  region has a land fraction larger than 1% or a no-retrieval fraction larger than 1%, then the cloud fraction for this  $17.6 \text{ km} \times 17.6 \text{ km}$  region will not be taken into the calculation of the total cloud fraction.

- 4) Examine the cloud fraction as a function of view angle. A scene will be flagged as a PPS if any of the following conditions are satisfied:
  - (i) Cameras with a view angle of  $70.5^\circ$  detect less cloud than cameras with a view angle of  $45.6^\circ$ .
  - (ii) Cameras with a view angle of  $60^\circ$  detect less cloud than cameras with a view angle of  $26.1^\circ$ .
  - (iii) The difference in cloud fraction between two adjacent cameras is larger than a predetermined tolerance  $\varepsilon_1$ .
  - (iv) The difference in cloud fraction between the DF camera and the DA camera is larger than a predetermined tolerance  $\varepsilon_2$ .

If the  $F_\theta$  algorithm flags a five-block scene as PPS, visual inspection on the RCCM performance for that scene can be performed in order to determine what (if any) course of action should be done to improve the performance of the RCCM. Note that the  $F_\theta$  technique only provides a necessary, but not sufficient, condition to judge the MISR RCCM performance. In other words, scenes flagged as PPS must have problems, but scenes that are not flagged as PPS may also have problems. Thus, the other types of cloud mask evaluation listed in section 1 cannot be abandoned.

## 5. Experiments

The  $F_\theta$  technique was applied to 1547 MISR orbits, which cover the period from 12 December 2001 to 1 May 2002. The versions of the MISR cloud classifier product and RCCM used in the experiments were F01\_0001 and F01\_0010, respectively. Data were only processed between  $55^\circ\text{N}$  and  $55^\circ\text{S}$  to ensure that the experimental results were not influenced by ice-covered ocean. It turns out that the number of PPSs flagged by the  $F_\theta$  algorithm is very sensitive to the tolerances  $\varepsilon_1$  and  $\varepsilon_2$  within the algorithm. For example, if  $\varepsilon_1 = 0.02$  and  $\varepsilon_2 = 0.10$ , then 18% of the scenes will be flagged as PPSs. If  $\varepsilon_1 = 0.03$  and  $\varepsilon_2 = 0.15$ , then 10% of the scenes will be flagged as PPSs. Ideally, all scenes flagged as PPSs should be visually inspected. However, considering the time and labor one can spend on visual

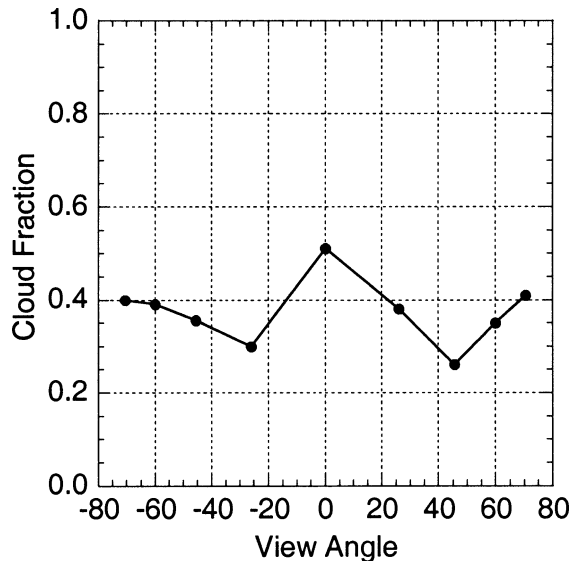


FIG. 3. Cloud fraction vs view angle for a sunglint-contaminated MISR scene flagged as PPS. MISR orbit 12 533, blocks 85–89, ~2355 UTC 26 Apr 2002.

inspection, we chose  $\varepsilon_1 = 0.05$  and  $\varepsilon_2 = 0.20$  to get 5% of the scenes flagged as PPSs. However, 5% of the total scenes is  $0.05 \times 1547$  (the number of the total orbits)  $\times 21$  (the number of five-block scenes per orbit between  $55^\circ\text{N}$  and  $55^\circ\text{S}$ ) = 1624 scenes, which still requires a large amount of time and labor for visual inspection. Because we anticipate only a handful of re-occurring problems in scenes labeled as PPSs, it suffices to sample those scenes labeled as PPSs. Scenes were evenly sampled in latitude, and after visually inspecting about 40 scenes, we noted that our conclusions were not changing. To be sure, we visually inspected and fully documented 88 PPSs. Major problems have been classified and summarized as follows.

### a. Sunglint

A sunglint-contaminated region is always difficult for cloud detection techniques, especially for techniques that only use solar channels. Sunglint dramatically increases the BRFs of clear pixels, which lowers the contrast in BRFs between cloudy and clear pixels. Additionally, the strength and distribution of sunglint depends on, for example, surface roughness, which varies from one scene to another. However, the RCCM ocean thresholds are static with relatively coarse sun-view geometry bins. Therefore, the RCCM cannot be expected to work perfectly over sunglint all the time.

Normally, sunglint only affects one or two cameras for a given five-block scene. For all of the sunglint cases that have been examined, a local peak always appears on the plot of cloud fraction versus view angle. For example, Fig. 3 shows a cloud fraction versus view angle plot for a five-block sunglint-contaminated scene.

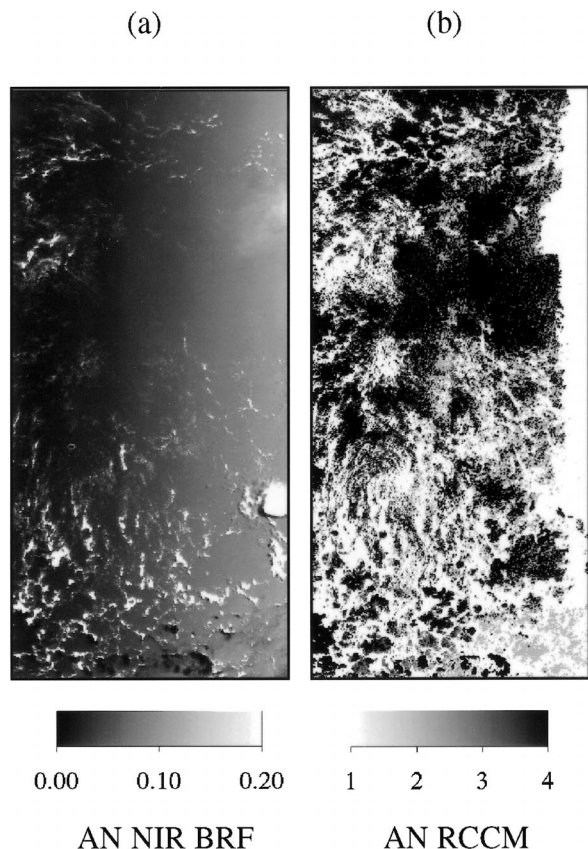


FIG. 4. (a) The NIR BRF image of the AN camera for MISR orbit 12 533, blocks 85–89. (b) The corresponding AN RCCM image: “1” represents high-confidence cloudy, “2” low-confidence cloudy, “3” low-confidence clear; and “4” high-confidence clear.

Notice the cloud fraction for the AN camera is larger than the AF and AA cameras. The associated NIR BRF and RCCM images for the AN camera are shown in Fig. 4. Clearly, sunglint covers much of the scene, and many clear pixels over sunglint are flagged as cloudy by the RCCM. Updating the few thresholds in the sun-view geometry bins over which sunglint may exist may not improve the RCCM performance because the sun-view geometry bins are very coarse and the thresholds are selected to perform well over a wide range of conditions. Thus, updating the thresholds when we have extreme sunglint may actually worsen the RCCM performance in other more typical sunglint conditions. Improving the quality of the RCCM over extreme sunglint is currently under investigation.

*b. Thin cirrus clouds/haze*

With the application of the  $F_{\theta}$  technique, 41 of the 88 PPSs visually inspected were found to have similar behaviors of cloud fraction versus view angle as the one shown in Fig. 5; namely, the cloud fractions show strong asymmetry between aft and forward cameras. In this case, the cloud fraction of the DF camera is 20% more

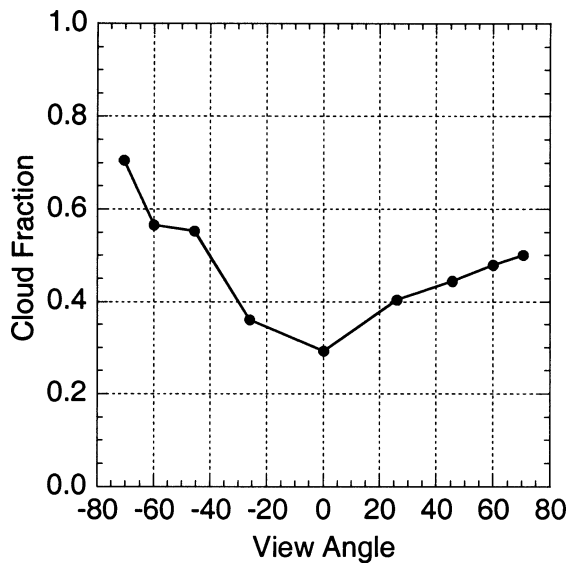


FIG. 5. Cloud fraction vs view angle for a scene flagged as PPS, but observed to be mostly covered by thin clouds. MISR orbit 11 438, blocks, 60–64, ~1930 UTC 10 Feb 2002.

than the DA camera, and the cloud fraction of the nadir camera is more than 20% less than the DA camera. For all 41 scenes, the BRF imagery shows a large portion of the scene covered by thin clouds or haze. For example, Fig. 6 shows the corresponding NIR BRF and the RCCM images for the AN camera for the case shown in Fig. 5. Our interpretation of the BRF image is that thin cirrus clouds cover a large portion of the scene. Large differences in cloud fractions between the DF and the DA cameras can be noticed by comparing the RCCM image of the DF camera with that of the DA camera in Fig. 6. The large difference in cloud fractions between the most oblique cameras and the nadir for a thin cloud-covered scene is mainly due to the fact that some clouds may be too thin to be detected by the nadir camera but can be detected by the oblique cameras because of the increased slant path through the cloud. The large difference of cloud fractions between the DF and the DA cameras is, however, much more interesting. We first did the obvious: tune the relevant thresholds. However, it turned out that the thresholds were near optimum; that is, when we compared the DF RCCM with the NIR BRF image for the DF camera, the results looked quite good. What we noted was that it was visually easier to see thin clouds in the DF camera NIR BRF image as compared with the DA camera BRF image, as shown in Fig. 7. This is because of the large radiative and spatial contrasts between the two viewing directions. In Fig. 7, the DF camera measures radiation that has been scattered into the forward-scatter direction (i.e., scattering angles  $< 90^\circ$ ), while the DA camera measures radiation that has been scattered into the backscatter direction (i.e., scattering angles  $> 90^\circ$ ). The large radiative contrast may exist because clouds tend to scatter more solar

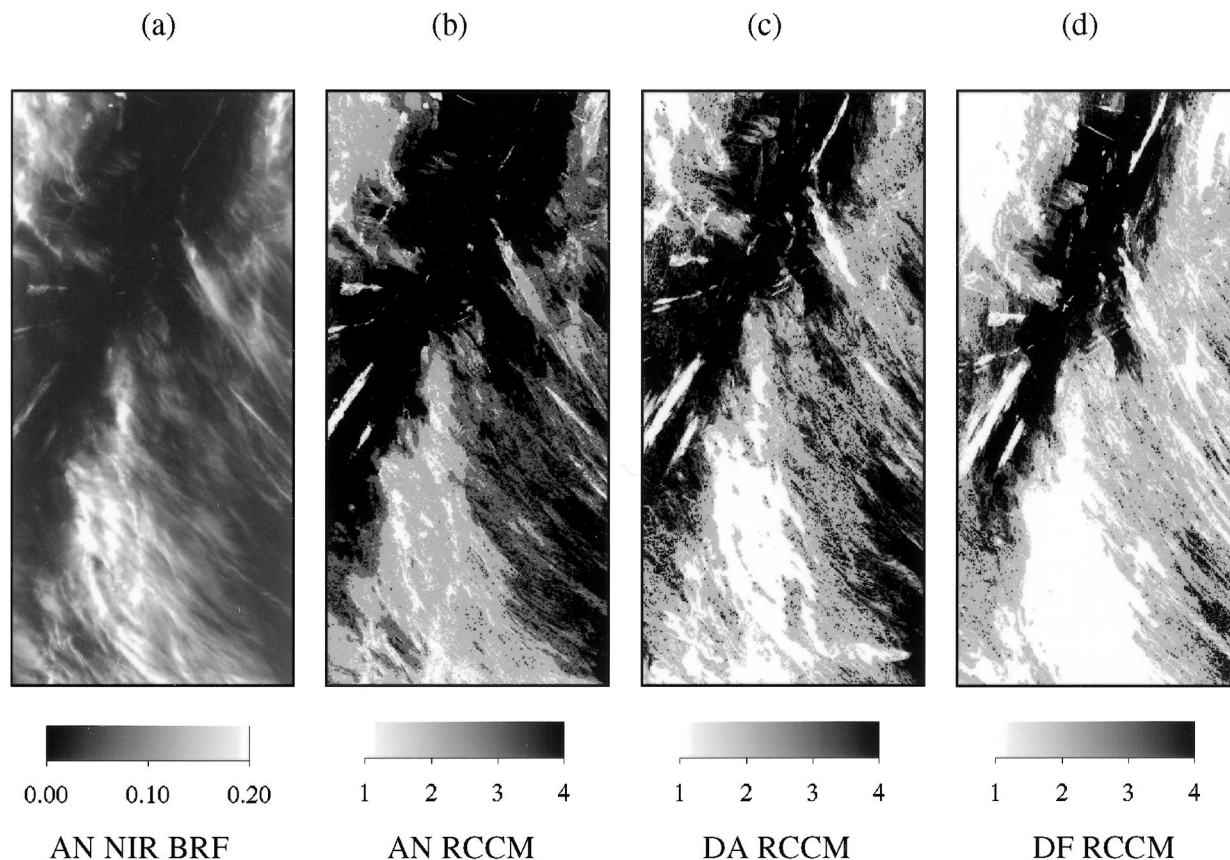


FIG. 6. (a) The NIR BRF image for the AN camera, MISR orbit 11 438, blocks 60–64, (b) the corresponding AN RCCM image, (c) the corresponding DA RCCM image, and (d) the corresponding DF RCCM image.

radiation into the forward direction compared to the backward direction. This leads to a larger contrast between clear sky and clouds over ocean in the forward direction. Additionally, the spatial contrast may exist because many more cloud shadows will appear when cameras view the clouds from the forward direction than from the backward direction. As a result,  $\sigma$  (see section 2) for cloudy pixels will on average be larger in the forward direction than in the backward direction, which will cause the RCCM of the camera viewing in the forward direction to flag more pixels as cloudy than the camera viewing in the backward direction. Therefore, as a result of radiative and spatial contrasts, some clouds may be thin enough to be undetectable in the DA camera, while being detectable in the DF camera in Fig. 7.

Another observation is that thick haze can have similar BRF values at the MISR channels and, to a lesser extent, spatial texture similar to very thin clouds. As a result, thick haze layers were observed to generate the same effect on the behavior of cloud fraction versus view angle as thin clouds. Hence, the  $F_\theta$  technique cannot distinguish thick haze from thin clouds. However, with the application of the  $F_\theta$  technique, a potentially simple algorithm may be set up to automatically flag a scene as dominantly covered by thin clouds/haze, for

example, by flagging large differences between the DF and DA cloud fractions. This is left to be demonstrated in future investigations.

The above conclusions are reflected in Figs. 8 and 9, which show scatterplots of the DF cloud fraction versus the AN and DA cloud fractions using all 1547 orbits of data over the Northern and Southern Hemispheres, respectively. As expected, the DF camera detects much more clouds than the AN camera in both the Northern and Southern Hemispheres. Also note that there are some cases where the DF camera detects fewer clouds than the AN camera, which is due to sunglint contaminating the AN camera. The number of such cases decreases as the AN cloud fraction increases, because the sunglint effect on the RCCM decreases with an increase in total cloud fraction.

Figures 8 and 9 also reveal that, on average, the DF camera detects more clouds than the DA camera over the Northern Hemisphere, but fewer clouds over the Southern Hemisphere. The reason is that the DF camera views largely forward-scattered radiation in the Northern Hemisphere and views largely backscattered radiation in the Southern Hemisphere. As discussed previously, the camera measuring forward-scattered radiation will detect more clouds than the camera measuring

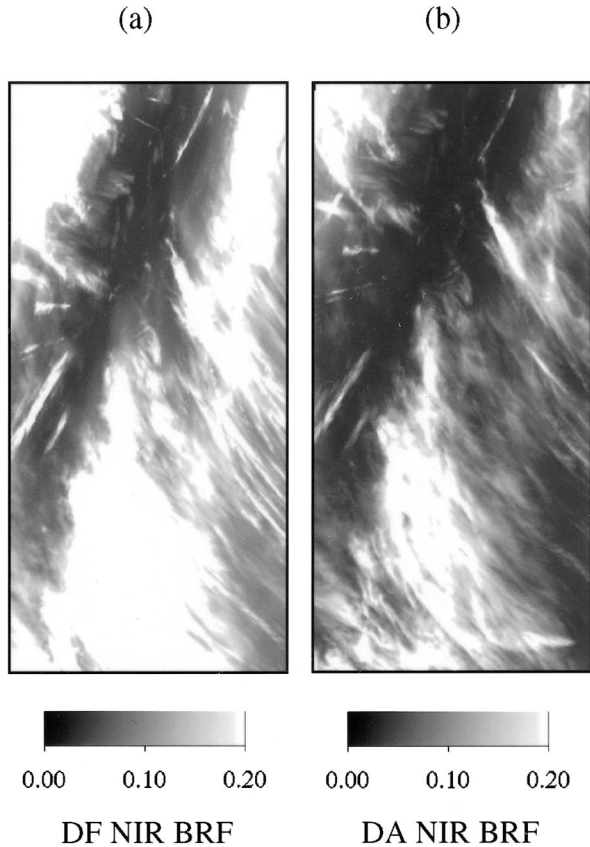


FIG. 7. (a) The NIR BRF image for the DF camera and (b) the corresponding DA NIR BRF image for MISR orbit 11 438, blocks 60–64, 33.1°–38.1°N latitude, 126.3°–127.8°W longitude. The scattering angles of the DF and DA cameras are  $\sim 68^\circ$  and  $\sim 141^\circ$ , respectively. Saturation of the images occurs for pixels having BRF values larger than 0.20, and they are displayed as white.

backscattered radiation, with the assumption that thresholds are properly set. Also note that the scatterplots of the DF versus AN cloud fractions are more biased toward the DF cloud fraction in the Northern Hemisphere than in the Southern Hemisphere. A possible reason is that there is more aerosol/haze (e.g., Husar et al. 1997) and thin cirrus (e.g., Wang et al. 1996) in the Northern Hemisphere than in the Southern Hemisphere. This may also be the reason that, on average, the difference in cloud fraction between the DF and DA cameras is larger in the Northern Hemisphere than in the Southern Hemisphere. These conclusions are only suggestive, because the RCCM has not been fully validated, and further in-depth analysis is required.

**6. Conclusions**

This article presents a unique approach called the  $F_\theta$  technique to evaluate in-scene performances of one of the MISR cloud masks, namely, the radiometric camera-by-camera cloud mask. The  $F_\theta$  technique is one of several approaches currently being used by the MISR Sci-

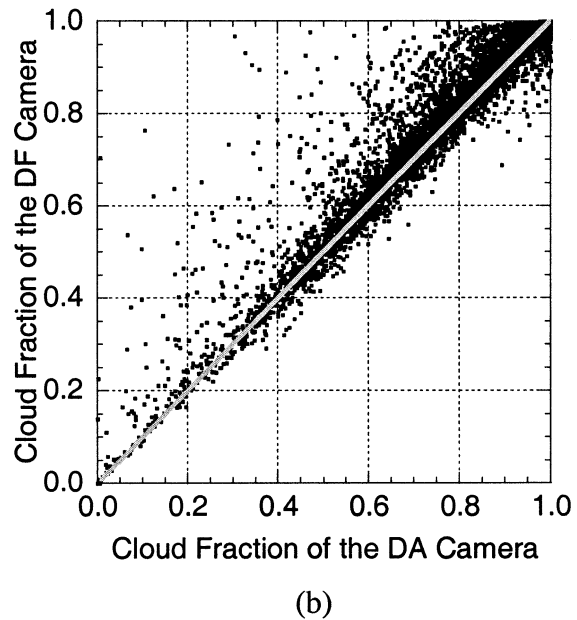
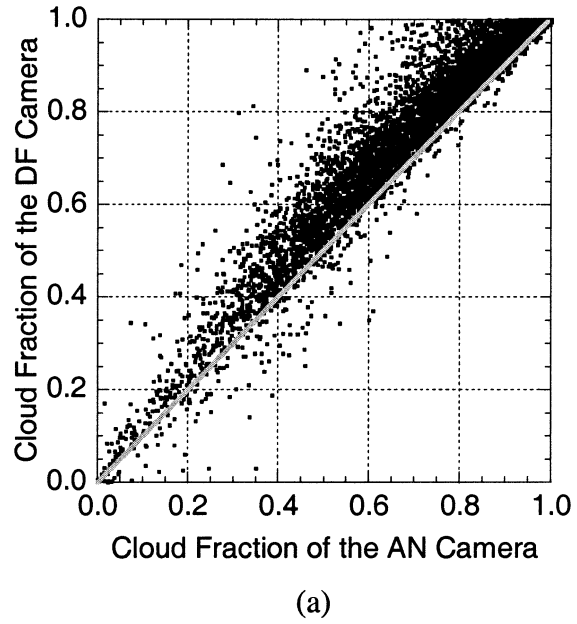


FIG. 8. Scatterplots of (a) the DF cloud fraction vs the AN cloud fraction, and (b) of the DF cloud fraction vs the DA cloud fractions for the Northern Hemisphere data only.

ence Team in aiding the validation of the RCCM by automatically and efficiently identifying potentially problematic scenes for further analysis. The results presented in this article were to demonstrate the application and utility of the  $F_\theta$  technique; they should not be construed as a final validation of the RCCM, because validation of the RCCM is an ongoing process. The results from the  $F_\theta$  technique applied to version F01\_0001 of the MISR cloud classifier and version F01\_0010 of the RCCM data will be used to examine ways to improve

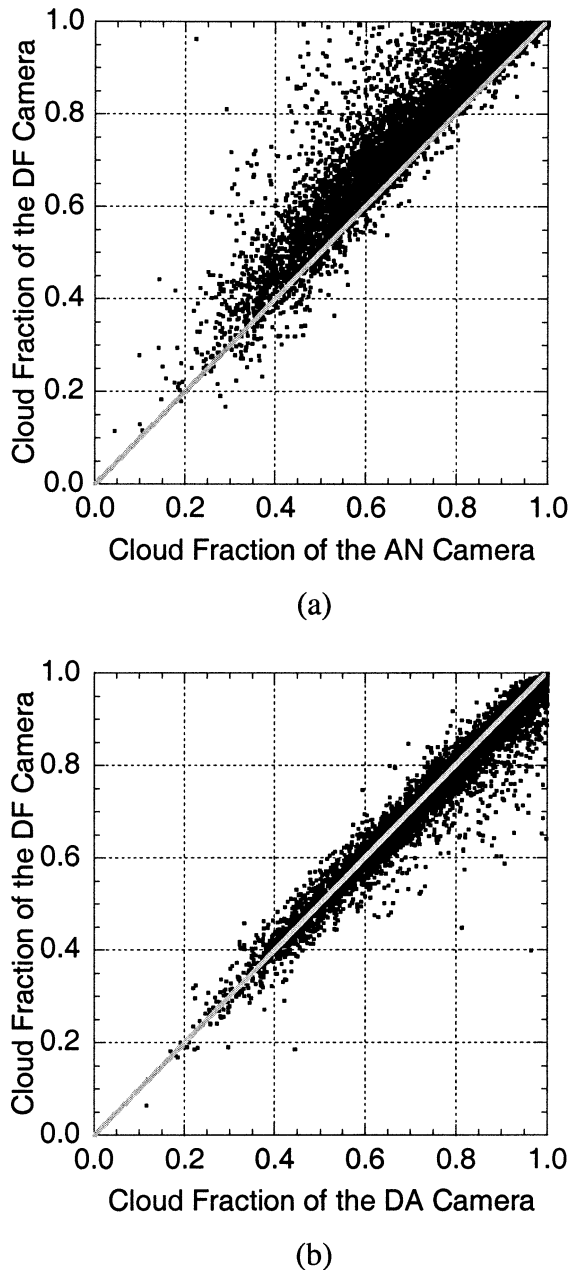


FIG. 9. The same as Fig. 8, but for the Southern Hemisphere data only.

the RCCM performance in later versions, in particular, over regions of sunglint and in distinguishing thin cirrus from thick haze. Once a new version of the RCCM is complete, the  $F_{\theta}$  technique will be applied to the new version for further assessment.

An examination of the cloud fraction versus view angle has also revealed a unique signature for the presence of thin cirrus or thick haze (see Fig. 5). This unique signature is asymmetric in the cloud fraction between the two most oblique cameras, namely, the DF and DA cameras. This was an unexpected result given that the viewing

zenith angle, hence, air mass, is the same for both cameras. The reason for the asymmetry may be the greater radiative and spatial contrast between clear and cloudy pixels that exists in the oblique views that measure radiation in the forward-scatter direction, as compared with oblique views that measure radiation in the backscatter direction. As a result, thinner clouds can be detected in views that measure radiation in the forward-scatter direction as compared with oblique views that measure radiation in the backscatter direction for a given air mass. It is our hypothesis that a similar effect must exist with other cloud detection techniques using radiative and spatial measures constructed from solar channels.

*Acknowledgments.* Partial support from the Jet Propulsion Laboratory of the California Institute of Technology under Contract 1221756 is gratefully acknowledged. Our sincere thanks are also extended to Jessica Lisiewski for her help in examining the MISR images and to three anonymous reviewers for suggested improvements to this manuscript. The MISR data were obtained from the NASA Langley Research Center Atmospheric Sciences Data Center.

#### REFERENCES

- Ackerman, S. A., K. Strabala, W. P. Menzel, R. A. Frey, C. C. Moeller, and L. E. Gumley, 1998: Discriminating clear sky from clouds with MODIS. *J. Geophys. Res.*, **103**, 32 141–32 158.
- Bothwell, G. W., E. G. Hansen, R. E. Vargo, and K. C. Miller, 2002: The Multi-angle Imaging SpectroRadiometer science data system, its products, tools and performances. *IEEE Trans. Geosci. Remote Sens.*, **40**, 1467–1476.
- Di Girolamo, L., and R. Davies, 1994: A band-differenced angular signature technique for cirrus cloud detection. *IEEE Trans. Geosci. Remote Sens.*, **32**, 890–896.
- , and —, 1997: Cloud fraction errors caused by finite resolution measurements. *J. Geophys. Res.*, **102**, 1739–1756.
- Diner, D. J., and Coauthors, 1998: Multi-angle Imaging SpectroRadiometer (MISR) description and experiment overview. *IEEE Trans. Geosci. Remote Sens.*, **36**, 1072–1087.
- , L. Di Girolamo, and E. Clothiaux, 1999: MISR level 1 cloud detection algorithm theoretical basis. Jet Propulsion Laboratory, JPL D-13397, Rev. B., 38 pp. [Available online at <http://eospsa.gsfc.nasa.gov/ftp-ATBD/REVIEW/MISR/ATBD-MISR-06/atbd-misr-06.pdf>.]
- , J. C. Beckert, G. W. Bothwell, and J. I. Rodriguez, 2002: Performance of the MISR instrument during its first 20 months in Earth orbit. *IEEE Trans. Geosci. Remote Sens.*, **40**, 1449–1466.
- Goodman, A. H., and A. Henderson-Sellers, 1988: Cloud detection and analysis: A review of recent progress. *Atmos. Res.*, **21**, 203–228.
- Gustafson, G. B., and Coauthors, 1994: Support of Environmental Requirements for Cloud Analysis and Archive (SERCAA): Algorithm descriptions. Phillips Laboratory, AFMC, Hanscom Air Force Base Rep. PL-TR-94-2114, 100 pp.
- Henderson-Sellers, A., and K. McGuffie, 1990: Are cloud amounts estimated from satellite sensor and conventional surface-based observations related? *Int. J. Remote Sens.*, **11**, 543–550.
- Husar, R. B., J. M. Prospero, and L. L. Stowe, 1997: Characterization of tropospheric aerosols over the oceans with the NOAA Advanced Very High Resolution Radiometer optical thickness operational product. *J. Geophys. Res.*, **102** (D14), 16 889–16 909.
- King, M. D., Y. J. Kaufman, W. P. Menzel, and D. Tanre, 1992: Remote sensing of cloud, aerosol, and water vapor properties

- from the Moderate Resolution Imaging Spectrometer (MODIS). *IEEE Trans. Geosci. Remote Sens.*, **30**, 2–15.
- McClain, E. P., 1989: Global sea surface temperatures and cloud clearing for aerosol optical depth estimates. *Int. J. Remote Sens.*, **10**, 763–769.
- Minnis, P., 1989: Viewing zenith angle dependence of cloudiness determined from coincident GOES East and GOES West data. *J. Geophys. Res.*, **94**, 2303–2320.
- , and E. F. Harrison, 1984: Diurnal variability of regional cloud and clear-sky radiative parameters derived from GOES data. Part I: Analysis method. *J. Climate Appl. Meteor.*, **23**, 993–1011.
- Platnick, S., M. D. King, S. Ackerman, W. P. Menzel, B. Baum, J. Riedi, and R. Frey, 2003: The MODIS cloud products: Algorithms and examples from terra. *IEEE Trans. Geosci. Remote Sens.*, **41**, 459–473.
- Snow, J. W., J. T. Bunting, R. P. d'Entremont, D. D. Grantham, K. R. Hardy, and E. M. Tomlinson, 1985: Space Shuttle cloud photographs assist in correcting meteorological satellite data. *Eos, Trans. Amer. Geophys. Union*, **66**, 489–490.
- Stowe, L., C. Wellemeier, T. Eck, H. Yeh, and the *Nimbus-7* Cloud Data Processing Team, 1988: *Nimbus-7* global cloud climatology. Part I: Algorithms and validation. *J. Climate*, **1**, 445–470.
- Tarpley, J. D., S. R. Schneider, and R. L. Money, 1984: Global vegetation indices from the *NOAA-7* meteorological satellite. *J. Climate Appl. Meteor.*, **23**, 491–494.
- Wang, P.-H., P. Minnis, M. P. McCormick, G. S. Kent, and K. M. Skeens, 1996: A 6-year climatology of cloud occurrence frequency from Stratospheric Aerosol and Gas Experiment II observations (1985–1990). *J. Geophys. Res.*, **101** (D23), 29 407–29 429.
- Wielicki, B. A., and L. Parker, 1992: On the determination of cloud cover from satellite sensors: The effect of sensor resolution. *J. Geophys. Res.*, **97**, 12 799–12 823.
- Zhao, G., 2003: Application of cloud fraction versus view angle relationships to validating the MISR cloud mask over the ocean. M.S. thesis, Dept. of Atmospheric Science, University of Illinois at Urbana–Champaign, 55 pp.